The structural style of intracontinental rift-inversion orogens

Dylan A. Vasey[1*], John B. Naliboff[2], Eric Cowgill[1], Sascha Brune[3,4], Anne Glerum[3], and Frank Zwaan[3,5]

[1]Department of Earth and Planetary Sciences, University of California, Davis, CA 95616

[2]Department of Earth and Environmental Science, New Mexico Institute of Mining and Technology, Socorro, NM 87801

[3]GFZ German Research Centre for Geosciences, Telegrafenberg, 14473 Potsdam, Germany

[4]Institute of Geosciences, University of Potsdam, 14476 Potsdam-Golm, Germany

[5]Department of Geosciences, University of Fribourg, 1700 Fribourg, Switzerland

** Now at Department of Earth and Climate Sciences, Tufts University, Medford, MA 02155 (Dylan.Vasey@tufts.edu)*

This manuscript is a non-peer reviewed preprint that has been submitted for publication in GEOLOGY. The manuscript has yet to be formally accepted for publication, and subsequent versions of this manuscript may have slightly different content. If accepted, the final version of this manuscript will be available via the "Peer-reviewed Publication DOI" link on the right-hand side of this webpage. Please feel free to contact any of the authors; we welcome feedback.

The structural style of intracontinental rift-inversion orogens

Dylan A. Vasey[1], John B. Naliboff[2], Eric Cowgill[1], Sascha Brune[3,4], Anne Glerum[3], and Frank Zwaan[3,5]

[1]Department of Earth and Planetary Sciences, University of California, Davis, CA 95616

[2]Department of Earth and Environmental Science, New Mexico Institute of Mining and Technology, Socorro, NM 87801

[3]GFZ German Research Centre for Geosciences, Telegrafenberg, 14473 Potsdam, Germany

[4]Institute of Geosciences, University of Potsdam, 14476 Potsdam-Golm, Germany

[5]Department of Geosciences, University of Fribourg, 1700 Fribourg, Switzerland

ABSTRACT

Although many collisional orogens result from subduction of oceanic lithosphere between two continents, some orogens form by strain localization within a continent via inversion of extensional structures inherited during continental rifting. Intracontinental rift-inversion orogens exhibit a wide range of first-order structural styles, but the underlying causes of such variability have not been extensively explored. Here, we use ASPECT to numerically model intracontinental rift inversion and investigate the impact on orogen structure of rift velocity/thermal structure, rift duration, post-rift cooling, and convergence velocity. Our models reproduce the natural variability of rift-inversion orogens, which can be categorized using three endmembers: asymmetric underthrusting (Style AU), distributed thickening (Style DT), and localized polarity flip (Style PF). Inversion of slow/cold rifts tends to produce orogens with more localized deformation (Styles AU and PF) than those resulting from host/fast rifts. However, multiple combinations of the parameters investigated here can produce the same structural style. Thus, there is not a unique relationship between orogenic structure and the conditions during and

prior to inversion. Because the structure of rift-inversion orogens is highly contingent upon the initial conditions prior to inversion, knowing the geologic history that preceded rift inversion is essential for translating orogenic structure into the processes that produced that structure.

INTRODUCTION

Plate-boundary collisional orogens form along long-lived boundaries between tectonic plates when two continental blocks collide following subduction of intervening oceanic lithosphere (e.g., Dewey and Bird, 1970). In contrast, intraplate orogens form within a continental plate by localization of strain along pre-existing weaknesses (e.g., Vilotte et al., 1982; Ziegler et al., 1995; Raimondo et al., 2014). Many intraplate orogens exploit weaknesses developed during continental rifting and thus are considered the result of rift inversion (Fig 1; e.g., Cooper et al., 1989; Beauchamp et al., 1996; Marshak et al., 2000). A common presumption seems to be that the first-order structural style of intracontinental rift-inversion orogens should be distinct from that of plate-boundary orogens, because during rift inversion convergence is expected to occur by reactivation of extensional structures, resulting in distributed lithospheric thickening (e.g., Buiter et al., 2009; Vincent et al., 2016, 2018). However, many rift-inversion orogens feature asymmetric underthrusting along lithosphere-scale shear zones and development of major fold-thrust systems (Fig. 1; e.g., Jammes et al., 2009), comparable to plate-boundary orogens (e.g., Willett et al., 1993; Beaumont et al., 1996).

Geodynamic numerical modeling of rift-inversion orogenesis typically focuses on the High Atlas and Pyrenees (e.g., Buiter et al., 2009; Jammes et al., 2014; Dielforder et al., 2019; Jourdon et al., 2019; Wolf et al., 2021), though the structural styles of these orogens are quite distinct (Fig. 1). The High Atlas is broadly symmetric, flanked on both sides by fold-thrust belts of opposing vergence, and exhibits no underthrusting of one block of lithosphere beneath another (e.g., Beauchamp et al., 1999; Gomez et al., 2000). In contrast, the Pyrenees show asymmetric lithospheric underthrusting and fold-thrust belt development concentrated on one side of the orogen (e.g., Muñoz, 1992; Dielforder et al., 2019). Other rift-inversion orogens exhibit a range of symmetry and thrust-belt vergence (Fig. 1; e.g., Greater Caucasus, Alice Springs, Araçuai-West Congo, Rocas Verdes; Philip et al., 1989; Fosdick et al., 2011; Raimondo et al., 2014; Fossen et al., 2020), but the controls on this variability are poorly understood.

Here, we present 2D geodynamic numerical models designed to explore connections between the initial conditions of an intracontinental rift prior to inversion and the structure of the resulting rift-inversion orogen. We find that permutations in rift velocity and thermal structure, rift duration, post-rift cooling, and inversion velocity dramatically change the first-order structure of the resulting orogen, producing models that exhibit the distributed lithospheric thickening of the High Atlas, the asymmetric lithospheric underthrusting of the Pyrenees, and additional variability reminiscent of other real-world rift inversion orogens. This study represents an attempt to explore a broad range of rift-inversion orogenic styles and highlights the sensitivity of rift-inversion orogens to changes in the initial conditions of the rift.

GEODYNAMIC MODELING OF RIFT-INVERSION OROGENESIS

We modeled 2D intracontinental rift inversion using the open-source, finite-element code ASPECT (Kronbichler et al., 2012; Heister et al., 2017; Naliboff et al., 2020; Bangerth et al., 2021; see the Supplemental Material for detailed methods[1]). To systematically compare the competing effects of rift velocity and thermal structure, rift duration, post-rift cooling, and convergence rate, we performed 16 model simulations in a 1000 x 600 km model domain (Fig. 2a, Table 1). Each model began by using different combinations of lithospheric thickness and extension velocity to develop either a slow/cold (narrow) or hot/fast (wide) rift from an initial block of continental lithosphere (Fig. 2b, Table 1; e.g., Tetreault and Buiter, 2018). We stopped extension either at lithospheric breakup or at half the model time required to reach lithospheric breakup. We inverted each of these four rift structures with either no post-rift cooling phase or after a cooling period of 20 Myr. For each of these eight models, we imposed two different convergence velocities during inversion (1 cm/yr, 5 cm/yr), with duration scaled (20 Myr, 4 Myr) so that each orogen underwent the same amount of total convergence (200 km).

RESULTING STYLES OF RIFT-INVERSION OROGENESIS

Style AU: Asymmetric Underthrusting

Several of our model rift-inversion orogens are characterized by distinctly asymmetric underthrusting of one block of lithosphere beneath another along a lithosphere-scale shear zone (Style AU, Fig. 2c). This behavior is exemplified by Model 1, formed from immediate inversion at 1 cm/yr of a slow/cold rift at halfway to lithospheric breakup (Fig. 2a; Table 1). In this model, initial symmetric uplift of both sides of the rift gives way to localization of most strain along a left-dipping shear zone to the right of the former rift axis (Fig. 2c). Near the end of the model run, deformation propagates both along a synthetic shear zone to the right of the main structure and along an antithetic backthrust to the left.

Style DT: Distributed Thickening

By contrast, a second subset of models does not localize deformation along lithosphere-scale thrust shear zones but instead undergoes distributed thickening of the lithosphere due to inversion along a broad set of former normal faults (Style DT). Model 5 (Fig. 2c) demonstrates this deformational style and tracks the immediate inversion at 1 cm/yr of a hot/ fast rift that has extended halfway to lithospheric breakup (Fig. 2a, Table 1). Distributed deformation during rifting leaves a ~400-km-wide zone of primarily upper-crustal normal faults with no distinct rift axis. Compression during inversion leads to reactivation of these structures as reverse faults while the lower crust and mantle lithosphere buckle and fold.

Style PF: Localized Polarity Flip

In a third set of models, deformation is localized asymmetrically along lithosphere-scale shear zones, but the individual shear zones are short-lived and are crosscut as new shear zones of opposite polarity take over (Style PF). An endmember demonstration of this orogenic style is Model 3 (Fig. 2c), which results from immediate inversion at 1 cm/yr of a slow/cold rift at full lithospheric breakup (Fig. 2a; Table 1). In this case, initial symmetric asthenospheric upwelling at the rift axis gives way to localized deformation along two right-dipping, lithosphere-scale shear zones that are then subsequently crosscut by left-dipping shear zones. The resulting orogen exhibits only a hint of right-directed vergence, with a subvertical, slightly left-dipping lithosphere-scale shear zone in the center of the orogen flanked by right- and left-directed thrust belts (Fig. 2c).

Intermediate Modes of Orogenic Style

Many of our model results can be classified as distinctly Style AU, DT, or PF rift-inversion orogens, while others exhibit orogenesis that is intermediate in character (Fig. 3). A good example is Model 6, which has equivalent parameters to Model 5 (Style DT exemplar, except that the rift is allowed to cool for 20 Myr prior to inversion (Fig. 2a; Table 1). During inversion, deformation is initially broadly distributed across both left- and right-dipping reactivated normal faults, but then right-dipping, lithosphere-scale shear zones begin to form and localize deformation in the final stages of inversion (Fig. 3). Thus, we classify this model as intermediate between Styles DT and AU.

Another example is Model 2, which results in a combination of Styles AU and PF (Fig. 3). This model is equivalent to Model 1 (Style AU exemplar) except for the addition of post-rift cooling (Table 1). Deformation is initially concentrated somewhat symmetrically along both left- and right-dipping shear zones and then becomes dominantly concentrated along the right-dipping zone before underthrusting of the lithosphere along a left-dipping lithosphere-scale shear zone takes over.

Model 4 is an example of intermediate behavior between Styles PF and DT. Except for the inclusion of post-rift cooling, Model 4 is equivalent to the Style PF exemplar Model 3 (Table 1). In Model 4, deformation is initially highly localized along a pair of antithetic shear zones extending from the relict rift axis (Fig. 3). As the rift basin closes, deformation is increasingly concentrated in a network of crustal-scale faults to accommodate crustal thickening, with some localization along left- and right-dipping shear zones.

CORRELATIONS BETWEEN INITIAL CONDITIONS AND OROGENIC STYLE

To visualize the relationship between the parameters differentiating our 16 model orogens and the resulting orogenic styles, we assign each model a place on a schematic ternary diagram with vertices representing Styles AU, DT, and PF (Fig. 3). The configuration of each individual orogen is highly contingent on the specific ensemble of parameters that produced it. However, there are some general patterns between individual parameters and our three endmember orogenic styles.

The greatest influence on orogenic style is exerted by the extensional velocity and thermal structure of the rift (Fig. 3). Rift-inversion orogens that start with a permutation of the slow/cold rift tend to have more localized deformation along lithosphere-scale shear zones, resulting in pronounced asymmetric underthrusting (Style AU) or flipping polarity (Style PF).

By contrast, inversion of a hot/fast rift tends to result in orogens with more distributed thickening (Style DT). However, this pattern does not hold across the full range of parameter space, with one slow/cold rift-inversion orogen (Model 4) exhibiting elements of distributed thickening (Style DT) and several hot/fast rift-inversion orogens (Models 6, 7, 8, 14, 15, 16) displaying at least some element of Styles AU or PF.

The influence of post-rift cooling and rift duration is less systematic. In general, cooling promotes increasing localization of deformation (Styles AU and PF). For slow/cold rift-inversion models, the post-rift cooling phase tends to result in shear zones of alternating polarity (Style PF) rather than asymmetric underthrusting (Style AU), whereas in hot, fast rift-inversion orogens, post-rift cooling tends to result in more distinctly asymmetric (Style AU) behavior (Fig. 3). Rifting to full lithospheric breakup rather than halfway to breakup promotes localized deformation (Styles AU and PF), though this is highly contingent on the rift velocity/temperature (Fig. 3). Full breakup in a slow/cold rift tends to promote Style PF over Style AU, whereas inversion of a hot/fast rift after full breakup promotes Style AU over Style DT.

The convergence velocity has the least impact on the structure of the resulting orogen. The most striking influence is seen by comparing Models 3 (1 cm/yr) and 11 (5 cm/yr), which are equivalent in setup apart from convergence velocity. Model 3 is our exemplar orogen for Style PF (Fig. 2c), whereas Model 11 exhibits asymmetric underthrusting representative of Style AU (Fig. 3).

COMPARISONS WITH PRIOR MODELING AND NATURAL EXAMPLES

In general, our results are consistent with prior modeling studies of rift inversion (see Supplementary Material for detailed comparisons with prior models[1]), in that studies focused on the Pyrenees tend to resemble Style AU and studies focused on the High Atlas tend to resemble

Style DT (e.g., Buiter et al., 2009; Jammes et al., 2014; Dielforder et al., 2019; Jourdon et al., 2019; Wolf et al., 2021). However, by exploring a wider range of first-order variations in initial rift conditions, we capture these two broad orogenic styles within a single suite of model results, in addition to other modes of deformation (Style PF and intermediate modes) that do not resemble the High Atlas or Pyrenees (Fig. 3).

This initial exploration demonstrates that the path to developing a particular structural style is non-unique; different combinations of rift velocity/temperature, rift duration, post-rift cooling, and/or convergence velocity can result in the same first-order style (Fig. 3). Thus, when examining natural intracontinental rift-inversion orogens, the observed structural style may provide some indication of initial conditions but cannot uniquely pinpoint a single set of conditions. For example, the distributed thickening (Style DT) characteristic of the High Atlas could result from closure of a short-duration, hot/fast rift with little to no post-rift cooling, whereas the asymmetric underthrusting (Style AU) in the Pyrenees could be caused by closure of a slow/cold rift approaching lithospheric breakup with a period of post-rift cooling (Figs. 1 and 3). However, the present-day structure of these orogens alone is insufficient to uniquely identify these parameters, so using additional observations to constrain their geologic histories is critical.

CONCLUSIONS

New 2D geodynamic numerical modeling of continental rift inversion indicates that the first-order structural style of rift-inversion orogens is highly dependent on initial conditions, including the extensional velocity/thermal structure of the rift, the extent of rifting, and the duration of post-rift cooling prior to inversion. Model orogens resulting from variation in these parameters and convergence velocity can be classified using three first-order structural styles: asymmetric underthrusting (Style AU), distributed thickening (Style DT), and localized polarity flip (Style PF). Interestingly, no systematic relationship exists between structural style and individual parameters, though slow/cold rifts, rifts that do not achieve lithospheric breakup, and rifts that cool prior to inversion tend to promote localized deformation (Styles AU and PF) over distributed deformation (Style DT). These model results reconcile the range of structural styles seen in natural rift-inversion orogens but also indicate that multiple sets of initial conditions can lead to a particular structural style.

ACKNOWLEDGMENTS

This material is based upon work supported by NSF grant EAR-2050623 to E. Cowgill. ASPECT is hosted by the Computational Infrastructure for Geodynamics (CIG), supported by NSF awards EAR-0949446 and EAR-1550901. This work used allocation EES210024 to E. Cowgill and CIG allocation EAR080022N on the Stampede2 cluster of the Texas Advanced Computing Center (TACC) at UT Austin, with access provided by XSEDE (Towns et al., 2014), supported by NSF grant ACI-1548562.

REFERENCES CITED

Bangerth, W., Dannberg, J., Fraters, M., Gassmoeller, R., Glerum, A., Heister, T., and Naliboff, J., 2021, ASPECT v2.3.0:, https://doi.org/10.5281/ZENODO.5131909.

Beauchamp, W., Allmendinger, R.W., Barazangi, M., Demnati, A., Alji, M.E., and Dahmani, M., 1999, Inversion tectonics and the evolution of the High Atlas Mountains, Morocco, based on a geological-geophysical transect: Tectonics, v. 18, p. 163–184, doi:10.1029/1998TC900015.

Beauchamp, W., Barazangi, M., Demnati, A., and Alji, M.E., 1996, Intracontinental Rifting and Inversion: Missour Basin and Atlas Mountains, Morocco: AAPG Bulletin, v. 80, p. 1459–1481, doi:10.1306/64ED9A60-1724-11D7-8645000102C1865D.

Beaumont, C., Ellis, S., Hamilton, J., and Fullsack, P., 1996, Mechanical model for subduction-collision tectonics of Alpine-type compressional orogens: Geology, v. 24, p. 675–678, doi:10.1130/0091-7613(1996)024<0675:MMFSCT>2.3.CO;2.

Buiter, S.J.H., Pfiffner, O.A., and Beaumont, C., 2009, Inversion of extensional sedimentary basins: A numerical evaluation of the localisation of shortening: Earth and Planetary Science Letters, v. 288, p. 492–504, doi:10.1016/j.epsl.2009.10.011.

Cooper, M.A., Williams, G.D., Graciansky, P.C. de, Murphy, R.W., Needham, T., Paor, D. de, Stoneley, R., Todd, S.P., Turner, J.P., and Ziegler, P.A., 1989, Inversion tectonics - A discussion: Geological Society, London, Special Publications, v. 44, p. 335–347, doi:10.1144/GSL.SP.1989.044.01.18.

Dewey, J.F., and Bird, J.M., 1970, Mountain belts and the new global tectonics: Journal of Geophysical Research, v. 75, p. 2625–2647, doi:10.1029/JB075i014p02625.

Dielforder, A., Frasca, G., Brune, S., and Ford, M., 2019, Formation of the Iberian-European convergent plate boundary fault and its effect on intraplate deformation in Central Europe: Geochemistry, Geophysics, Geosystems, v. 20, p. 2395–2417, doi:10.1029/2018GC007840.

Fosdick, J.C., Romans, B.W., Fildani, A., Bernhardt, A., Calderón, M., and Graham, S.A., 2011, Kinematic evolution of the Patagonian retroarc fold-and-thrust belt and Magallanes foreland basin, Chile and Argentina, 51°30′S: GSA Bulletin, v. 123, p. 1679–1698, doi:10.1130/B30242.1.

Fossen, H., Cavalcante, C., Konopásek, J., Meira, V.T., de Almeida, R.P., Hollanda, M.H.B.M., and Trompette, R., 2020, A critical discussion of the subduction-collision model for the Neoproterozoic Araçuaí-West Congo orogen: Precambrian Research, v. 343, p. 105715, doi:10.1016/j.precamres.2020.105715.

Gomez, F., Beauchamp, W., and Barazangi, M., 2000, Role of the Atlas Mountains (northwest Africa) within the African-Eurasian plate-boundary zone: Geology, v. 28, p. 775–778, doi:10.1130/0091-7613(2000)28<775:ROTAMN>2.0.CO;2.

Heister, T., Dannberg, J., Gassmöller, R., and Bangerth, W., 2017, High accuracy mantle convection simulation through modern numerical methods – II: realistic models and problems: Geophysical Journal International, v. 210, p. 833–851, doi:10.1093/gji/ggx195.

Jammes, S., Huismans, R.S., and Muñoz, J.A., 2014, Lateral variation in structural style of mountain building: controls of rheological and rift inheritance: Terra Nova, v. 26, p. 201–207, doi:10.1111/ter.12087.

Jammes, S., Manatschal, G., Lavier, L., and Masini, E., 2009, Tectonosedimentary evolution related to extreme crustal thinning ahead of a propagating ocean: Example of the western Pyrenees: Tectonics, v. 28, doi:https://doi.org/10.1029/2008TC002406.

Jourdon, A., Le Pourhiet, L., Mouthereau, F., and Masini, E., 2019, Role of rift maturity on the architecture and shortening distribution in mountain belts: Earth and Planetary Science Letters, v. 512, p. 89–99, doi:10.1016/j.epsl.2019.01.057.

Kronbichler, M., Heister, T., and Bangerth, W., 2012, High accuracy mantle convection simulation through modern numerical methods: Geophysical Journal International, v. 191, p. 12–29, doi:10.1111/j.1365-246X.2012.05609.x.

Marshak, S., Karlstrom, K., and Timmons, J.M., 2000, Inversion of Proterozoic extensional faults: An explanation for the pattern of Laramide and Ancestral Rockies intracratonic deformation, United States: Geology, v. 28, p. 735–738, doi:10.1130/0091-7613(2000)28<735:IOPEFA>2.0.CO;2.

Muñoz, J.A., 1992, Evolution of a continental collision belt: ECORS-Pyrenees crustal balanced cross-section, *in* McClay, K.R. ed., Thrust Tectonics, Dordrecht, Springer Netherlands, p. 235–246, doi:10.1007/978-94-011-3066-0_21.

Naliboff, J.B., Glerum, A., Brune, S., Péron-Pinvidic, G., and Wrona, T., 2020, Development of 3-D Rift Heterogeneity Through Fault Network Evolution: Geophysical Research Letters, v. 47, p. e2019GL086611, doi:https://doi.org/10.1029/2019GL086611.

Philip, H., Cisternas, A., Gvishiani, A., and Gorshkov, A., 1989, The Caucasus: An actual example of the initial stages of continental collision: Tectonophysics, v. 161, p. 1–21, doi:10.1016/0040-1951(89)90297-7.

Raimondo, T., Hand, M., and Collins, W.J., 2014, Compressional intracontinental orogens: Ancient and modern perspectives: Earth-Science Reviews, v. 130, p. 128–153, doi:10.1016/j.earscirev.2013.11.009.

Tetreault, J.L., and Buiter, S.J.H., 2018, The influence of extension rate and crustal rheology on the evolution of passive margins from rifting to break-up: Tectonophysics, v. 746, p. 155–172, doi:10.1016/j.tecto.2017.08.029.

Towns, J. et al., 2014, XSEDE: Accelerating Scientific Discovery: Computing in Science & Engineering, v. 16, p. 62–74, doi:10.1109/MCSE.2014.80.

Vilotte, J.P., Daignières, M., and Madariaga, R., 1982, Numerical modeling of intraplate deformation: Simple mechanical models of continental collision: Journal of Geophysical Research: Solid Earth, v. 87, p. 10709–10728, doi:https://doi.org/10.1029/JB087iB13p10709.

Vincent, S.J., Braham, W., Lavrishchev, V.A., Maynard, J.R., and Harland, M., 2016, The formation and inversion of the western Greater Caucasus Basin and the uplift of the western Greater Caucasus: Implications for the wider Black Sea region: Tectonics, v. 35, p. 2948–2962, doi:10.1002/2016TC004204.

Vincent, S.J., Saintot, A., Mosar, J., Okay, A.I., and Nikishin, A.M., 2018, Comment on “Relict basin closure and crustal shortening budgets during continental collision: An example from Caucasus sediment provenance” by Cowgill et al. (2016): Tectonics, v. 37, p. 1006–1016, doi:10.1002/2017TC004515.

Willett, S., Beaumont, C., and Fullsack, P., 1993, Mechanical model for the tectonics of doubly vergent compressional orogens: Geology, v. 21, p. 371–374, doi:10.1130/0091-7613(1993)021<0371:MMFTTO>2.3.CO;2.

Wolf, S.G., Huismans, R.S., Muñoz, J.-A., Curry, M.E., and Beek, P. van der, 2021, Growth of Collisional Orogens From Small and Cold to Large and Hot—Inferences From Geodynamic Models: Journal of Geophysical Research: Solid Earth, v. 126, p. e2020JB021168, doi:https://doi.org/10.1029/2020JB021168.

Ziegler, P.A., Cloetingh, S., and van Wees, J.-D., 1995, Dynamics of intra-plate compressional deformation: the Alpine foreland and other examples: Tectonophysics, v. 252, p. 7–59, doi:10.1016/0040-1951(95)00102-6.

FIGURE CAPTIONS

Figure 1: Schematic cross-sections of Cenozoic and Pre-Cenozoic rift-inversion orogens ordered by degree of symmetry (adapted from Raimondo et al., 2014; Fossen et al., 2020; Fosdick et al., 2011; Beauchamp et al., 1999; Dielforder et al., 2019; Philip et al., 1989).

Figure 2: a) Graphical overview of parameter space explored by the 16 models in this study. An initial slow/cold or hot/fast rift is taken either halfway or all the way to lithospheric breakup. The resulting 4 rift structures (color-coded, see Fig. 2b) are either inverted immediately (saturated colors) or after 20 Myr of post-rift cooling (faded colors) at either a slower (1 cm/yr; no underline) or faster (5 cm/yr; underlined) convergence rate. **b)** Initial conditions for the model orogens prior to inversion, indicating variations in rift temperature and velocity, as well as post-rift cooling. **c)** Rift inversion results from exemplar model orogens for each of the three structural styles discussed in the text, shown prior to inversion, after 100 km of convergence, and after 200 km of convergence.

Figure 3: Schematic ternary diagram indicating first-order structural style of each model orogen. Model results shown with ticks at 300 and 700 km on the x axis and 400 and 600 km on the y axis (i.e., the same model area as panels in Fig. 2). Double-headed arrow indicates that rift temperature and velocity exhibit the strongest control on structural style. Natural examples of rift-inversion orogens are also plotted, showing a similar spread in structural style.

[1]Supplemental Material. Methods, additional tables/figures, and videos of model runs. Please visit https://doi.org/10.1130/XXXX to access the supplemental material, and contact editing@geosociety.org with any questions.

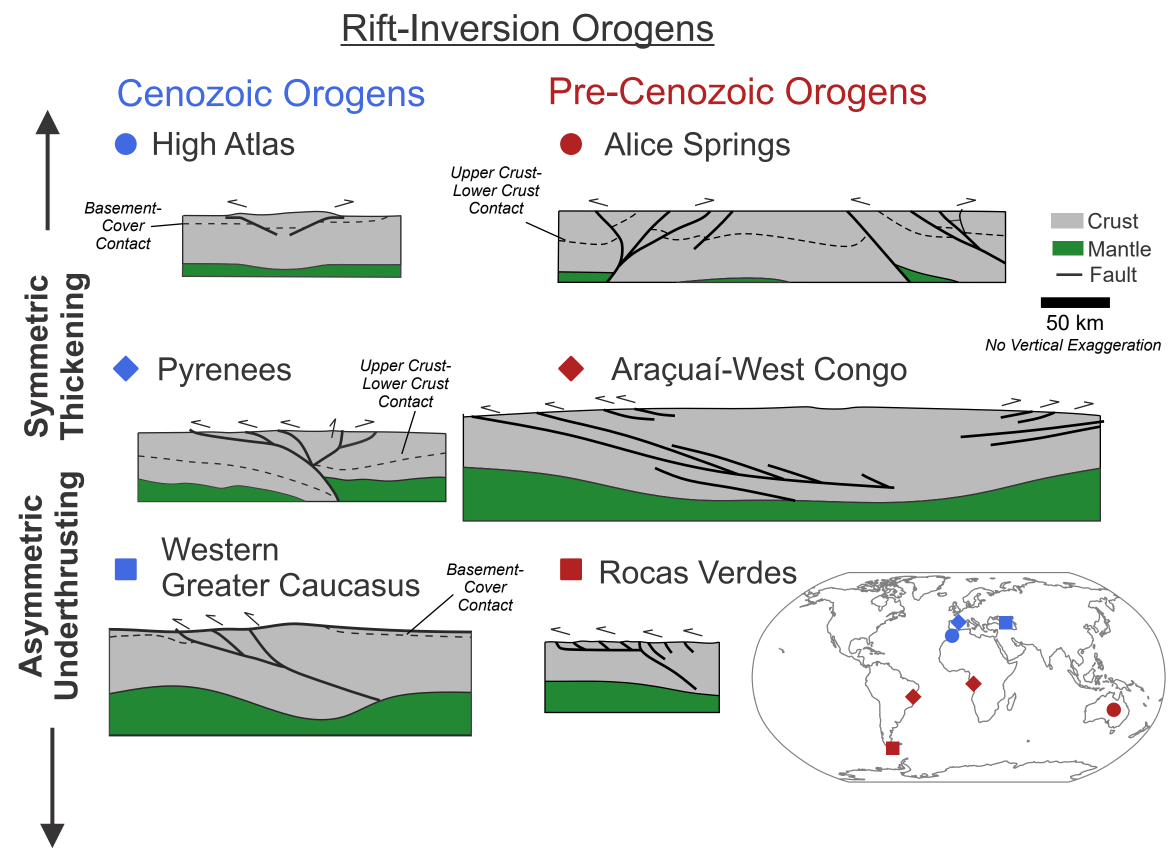
Rift-Inversion Orogens
Cenozoic Orogens
Pre-Cenozoic Orogens
Symmetric Thickening
Asymmetric Underthrusting
High Atlas
Basement-Cover Contact
Alice Springs
Upper Crust-Lower Crust Contact
Crust
Mantle
Fault
50 km
No Vertical Exaggeration
Pyrenees
Upper Crust-Lower Crust Contact
Araçuaí-West Congo
Western Greater Caucasus
Basement-Cover Contact
Rocas Verdes

Figure 1

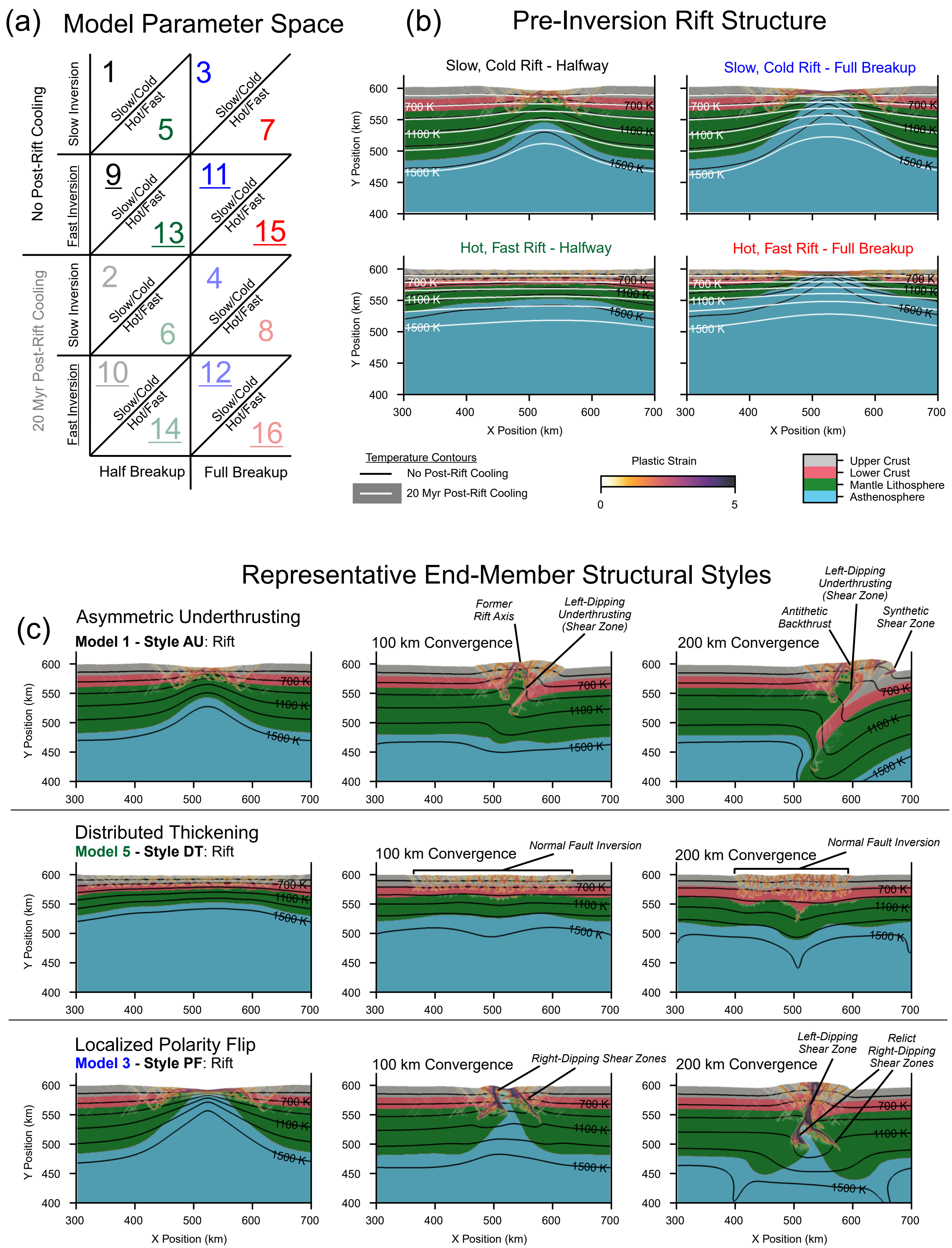
(a) Model Parameter Space
No Post-Rift Cooling
20 Myr Post-Rift Cooling
Slow Inversion
Fast Inversion
Slow/Cold
Hot/Fast
1
3
5
7
9
11
13
15
2
4
6
8
10
12
14
16
Half Breakup
Full Breakup
(b) Pre-Inversion Rift Structure
Slow, Cold Rift - Halfway
Slow, Cold Rift - Full Breakup
Hot, Fast Rift - Halfway
Hot, Fast Rift - Full Breakup
Y Position (km)
X Position (km)
700 K
1100 K
1500 K
Temperature Contours
No Post-Rift Cooling
20 Myr Post-Rift Cooling
Plastic Strain
0
5
Upper Crust
Lower Crust
Mantle Lithosphere
Asthenosphere
Representative End-Member Structural Styles
(c)
Asymmetric Underthrusting
Model 1 - Style AU: Rift
100 km Convergence
200 km Convergence
Former Rift Axis
Left-Dipping Underthrusting (Shear Zone)
Antithetic Backthrust
Synthetic Shear Zone
Distributed Thickening
Model 5 - Style DT: Rift
Normal Fault Inversion
Localized Polarity Flip
Model 3 - Style PF: Rift
Right-Dipping Shear Zones
Left-Dipping Shear Zone
Relict Right-Dipping Shear Zones

Figure 2

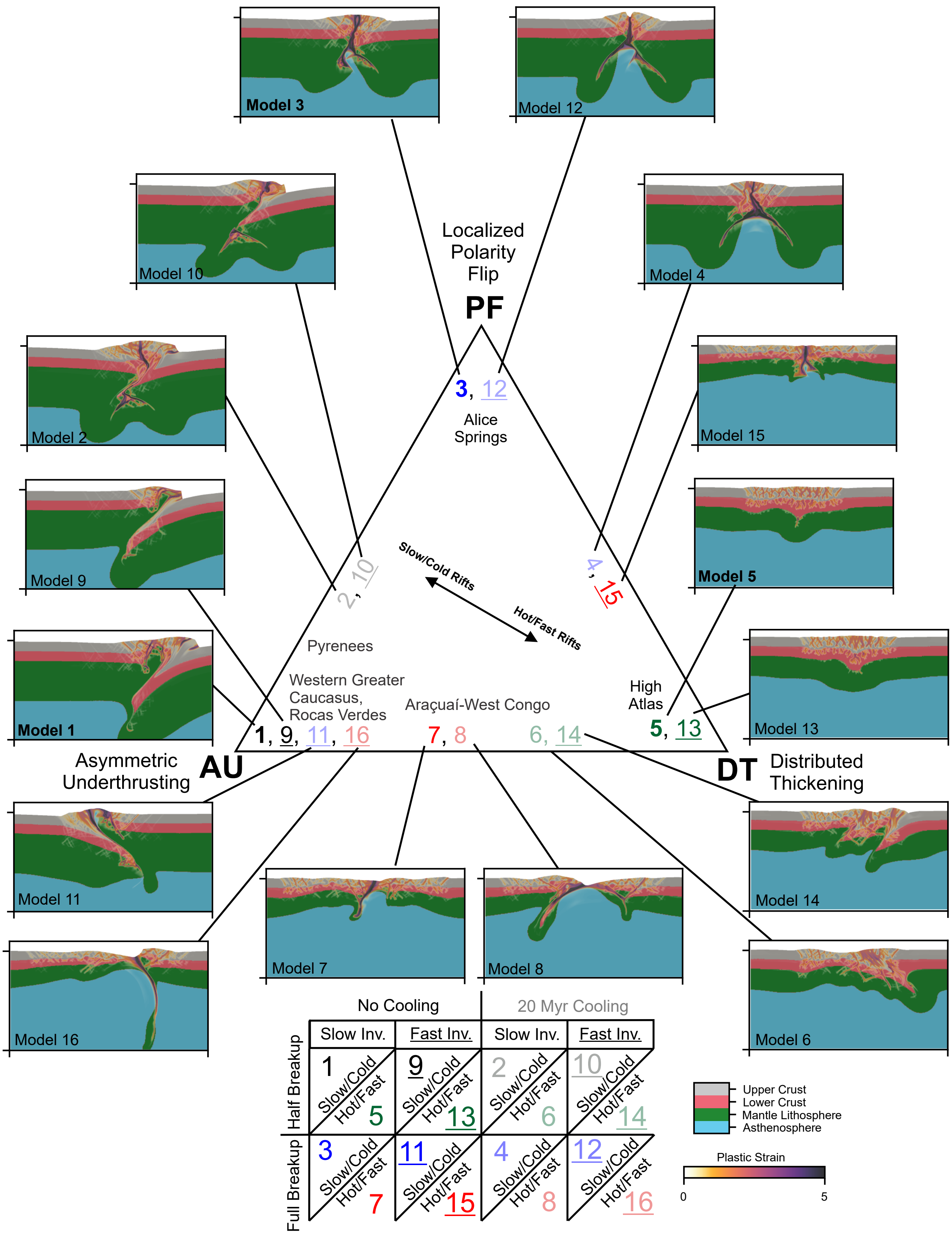
Model 3
Model 12
Model 10
Model 4
Localized
Polarity
Flip
PF
Model 2
Model 15
3, 12
Alice
Springs
Model 9
Model 5
Slow/Cold Rifts
Hot/Fast Rifts
2, 10
4, 15
Pyrenees
Model 1
Model 13
Western Greater
Caucasus,
Rocas Verdes
Araçuaí-West Congo
High
Atlas
1, 9, 11, 16
7, 8
6, 14
5, 13
Asymmetric
Underthrusting
AU
DT
Distributed
Thickening
Model 11
Model 14
Model 7
Model 8
Model 16
Model 6
No Cooling
20 Myr Cooling
Slow Inv.
Fast Inv.
Slow Inv.
Fast Inv.
Half Breakup
Full Breakup
1 Slow/Cold Hot/Fast 5
9 Slow/Cold Hot/Fast 13
2 Slow/Cold Hot/Fast 6
10 Slow/Cold Hot/Fast 14
3 Slow/Cold Hot/Fast 7
11 Slow/Cold Hot/Fast 15
4 Slow/Cold Hot/Fast 8
12 Slow/Cold Hot/Fast 16
Upper Crust
Lower Crust
Mantle Lithosphere
Asthenosphere
Plastic Strain
0
5

Figure 3

Table 1: Summary of Rift Inversion Model Parameters

Model Number	Model ID	Extension Velocity	Lithosphere Thickness	Rift Duration	Post-Rift Cooling	Inversion Velocity	Inversion Duration	Total Model Duration
1	063022_rip_c	0.5 cm/yr	120 km	Halfway (16 Myr)	0 Myr	1 cm/yr	20 Myr	36 Myr
2	071822_rip_b	0.5 cm/yr	120 km	Halfway (16 Myr)	20 Myr	1 cm/yr	20 Myr	56 Myr
3	070422_rip_e	0.5 cm/yr	120 km	Full Breakup (32 Myr)	0 Myr	1 cm/yr	20 Myr	52 Myr
4	072022_rip_a	0.5 cm/yr	120 km	Full Breakup (32 Myr)	20 Myr	1 cm/yr	20 Myr	72 Myr
5	070422_rip_c	2 cm/yr	80 km	Halfway (7.3 Myr)	0 Myr	1 cm/yr	20 Myr	27.3 Myr
6	071322_rip	2 cm/yr	80 km	Halfway (7.3 Myr)	20 Myr	1 cm/yr	20 Myr	47.3 Myr
7	070622_rip_a	2 cm/yr	80 km	Full Breakup (14.5 Myr)	0 Myr	1 cm/yr	20 Myr	34.5 Myr
8	072022_rip_b	2 cm/yr	80 km	Full Breakup (14.5 Myr)	20 Myr	1 cm/yr	20 Myr	54.5 Myr
9	080122_rip_a	0.5 cm/yr	120 km	Halfway (16 Myr)	0 Myr	5 cm/yr	3.4 Myr*	19.4 Myr
10	080122_rip_e	0.5 cm/yr	120 km	Halfway (16 Myr)	20 Myr	5 cm/yr	3.5 Myr*	39.5 Myr
11	080122_rip_b	0.5 cm/yr	120 km	Full Breakup (32 Myr)	0 Myr	5 cm/yr	4 Myr	36 Myr
12	080122_rip_f	0.5 cm/yr	120 km	Full Breakup (32 Myr)	20 Myr	5 cm/yr	4 Myr	56 Myr
13	080122_rip_c	2 cm/yr	80 km	Halfway (7.3 Myr)	0 Myr	5 cm/yr	4 Myr	11.3 Myr
14	080122_rip_g	2 cm/yr	80 km	Halfway (7.3 Myr)	20 Myr	5 cm/yr	4 Myr	31.3 Myr
15	080122_rip_d	2 cm/yr	80 km	Full Breakup (14.5 Myr)	0 Myr	5 cm/yr	4 Myr	18.5 Myr
16	080122_rip_h	2 cm/yr	80 km	Full Breakup (14.5 Myr)	20 Myr	5 cm/yr	4 Myr	38.5 Myr

*Models 9 and 10 failed to numerically converge prior to completion of the inversion stage and did not experience the full 200 km of inversion.

The structural style of intracontinental rift-inversion orogens

Dylan A. Vasey, John B. Naliboff, Eric Cowgill, Sascha Brune, Anne Glerum, Frank Zwaan

Supplemental Material

Contents of This Document:

Text S1
Tables S1 and S2
Figures S1-S3

Separate Files:

Videos of each model rift inversion orogen (Models 1-16) showing compositional field/temperature (same color scheme and contours as Figs. 2-3), plastic strain, strain rate, and viscosity over time.

Text S1

Numerical Methods

We model 2D continental rift inversion using the open-source, finite-element code ASPECT (Advanced Solver for Problems in Earth's ConvecTion; Kronbichler et al., 2012; Heister et al., 2017; Bangerth et al., 2021), which has been used to model complex processes of lithospheric deformation in a variety of settings (e.g., Glerum et al., 2018, 2020; Fraters and Billen, 2021; Bahadori et al., 2022; Weerdesteijn et al., 2023; Heron et al., 2023; Brune et al., 2023). ASPECT solves equations throughout the model domain for the conservation of momentum, mass, and energy, as well as advection-diffusion equations. Velocity and pressure are solved for using the extended Boussinesq approximation, with the Stokes equations defined as:

$$\nabla \cdot u = 0$$

$$-\nabla \cdot 2\mu\dot{\epsilon}(u) + \nabla P = \rho g$$

Above, u is velocity, μ is viscosity, $\dot{\epsilon}$ is the deviatoric strain rate, P is pressure, ρ is density, and g is gravitational acceleration.

We model temperature evolution with a combination of advection, heat conduction, shear heating, and adiabatic heating:

$$\rho C_p \left(\frac{\partial T}{\partial t} + u \cdot \nabla T \right) - \nabla \cdot \kappa \nabla T = \rho H + 2\eta\dot{\epsilon}(u) + -\alpha\rho T(u \cdot g)$$

Here, C_p is heat capacity, T is temperature, t is time, κ is thermal diffusivity, α is the linear thermal expansion coefficient, and H is the rate of internal heating. The terms on the right side of the equation correspond to internal heat production, shear heating, and adiabatic heating, respectively.

Density varies linearly as a function of a reference density (ρ_0), a reference temperature (T_0), the linear expansion coefficient, and temperature:

$$\rho = \rho_0(1 - \alpha(T - T_0))$$

The rheological behavior combines nonlinear viscous flow with brittle failure (e.g., Glerum et al., 2018), with viscous flow in the crust and mantle lithosphere following a dislocation creep flow law:

$$\sigma'_{II} = A^{\frac{-1}{n}} \dot{\epsilon}_{II}^{\frac{1}{n}} e^{\frac{Q+PV}{nRT}}$$

In the asthenosphere, dislocation creep is harmonically averaged with a diffusion creep flow law:

$$\sigma'_{II} = A^{-1} \dot{\epsilon}_{II} d^{\frac{m}{n}} e^{\frac{Q+PV}{nRT}}$$

In these equations, $\sigma'_{II}$is the second invariant of deviatoric stress, A is a viscous prefactor, $n$is the stress exponent, $\dot{\epsilon}_{II}$ is the second invariant of the deviatoric strain rate, Q is activation energy, V is activation volume, R is the gas constant, d is grain size, and m is the grain size exponent.

Brittle plastic deformation follows a Drucker Prager yield criterion, which accounts for softening of the angle of internal friction (ϕ) and cohesion (C) as a function of accumulated plastic strain:

$$\sigma'_{II} = Psin(\phi) + Ccos(\phi)$$

For our models, the initial friction angle is 30° and cohesion is 20 MPa; these values linearly weaken by a factor 0.375 as a function of finite plastic strain.

Geodynamic Model Setup

Model Domain and Kinematic Boundary Conditions

The governing equations are solved on a 1000 km by 600 km grid with a resolution of 1 km below the temperature corresponding to a depth of 150 km at the model start, 2 km resolution between 150 and 250 km, and 4 km resolution at temperatures corresponding to depths greater than 250 km at the model start. Such coarsening of the model resolution as a function of temperature ensures the lithosphere and uppermost asthenosphere maintain the same numerical resolution, while also significantly decreasing simulation run times. Significantly, we note that the final stages of the rift inversion and resulting orogen structures are highly sensitive to the adaptive mesh refinement criterion, and we conducted extensive sensitivity tests to ensure our criterion produces the same results as models with constant numerical resolutions, as discussed below.

Deformation is driven by imposing horizontal velocities on the model sides, with inflow/outflow in the top half of the model balanced by equivalent outflow/inflow in the bottom half of the model (Fig. S1). To simulate rift inversion, we first apply a constant extensional velocity to simulate rifting, followed by a period of no velocity to simulate post-rift cooling and then a period of constant convergent velocity to simulate inversion and orogenesis. Varying the magnitude and sign of the boundary velocity terms governs these distinct stages of deformation. The initial extension phase is designed using previous models of long-term continental rifting in ASPECT (e.g., Naliboff et al., 2020; Glerum et al., 2020; Gouiza and Naliboff, 2021; Magni et al., 2021; Brune et al., 2023). The bottom boundary permits free slip and the top boundary is a free surface (Rose et al., 2017), allowing development of topography over time. Erosion and sedimentation on the free surface are approximated using hillslope diffusion (Sandiford et al., 2021).

Initial Thermal Structure and Thermal Evolution

The initial geothermal structure blends a conductive cooling profile within the lithosphere (Chapman, 1986) with an approximated adiabatic temperature profile that dominates temperature gradients in the convecting mantle. Following previous continental rift models (Naliboff et al., 2017, 2020), we produce a conductive lithospheric temperature profile by prescribing a surface heat flow value that is used to calculate the change in temperature with depth using the thermodynamic properties of each lithospheric layer (Fig. S1). When combined with the approximated adiabatic profile, the surface heat flow can be adjusted to produce a desired lithospheric thickness (e.g., Magni et al., 2021), the base of which is defined by the 1300°C isotherm.

Lithologic Structure and Rheology

The model domain contains distinct compositional layers with unique thermodynamic (density, radiogenic heating) and rheologic (flow law) properties (Table S1, Fig. S1). Each layer and additional advected non-lithologic fields (e.g., strain) are tracked using particle-in-cell methods. Following previous models of continental rifting (Naliboff and Buiter, 2015; Naliboff et al., 2017, 2020), an initial 40 km crust is evenly divided into upper (2800 kg/m^3) and lower (2900 kg/m^3) layers, following wet quartzite (Gleason and Tullis, 1995) and wet anorthite (Rybacki et al., 2006) dislocation creep flow laws, respectively. Although the crustal lithologic structure is held constant, the bulk rheology of the crust (and mantle) varies as a function of the initial geothermal structure.

The mantle (3300 kg/m^3) viscous rheology is defined using flow laws for dry olivine (Hirth and Kohlstedt, 2003), with dislocation creep only in the mantle lithosphere and a composite of dislocation and diffusion creep in the asthenosphere (Table S1). Deformation during the initial stages of rifting is localized in the model center by delineating a 250 x 60 km zone of heterogeneous initial plastic strain (Fig. S1; after Pan et al., 2022).

Experimental Approach

We ran 16 rift-inversion models in 2D (Table 1). Each model began by developing either a narrow or wide rift from the initial block of continental lithosphere using variations in lithospheric strength and extension velocity. We adjusted lithospheric strength by changing the surface heat flow, which changes the geothermal gradient and thus the thickness of the mantle lithosphere, defined by a lithosphere-asthenosphere boundary (LAB) at the 1300°C isotherm. We created a narrow rift by slowly (0.5 cm/yr) extending a cold, thick lithosphere (120 km total, 80 km mantle lithosphere) and a wide rift by rapidly (2 cm/yr) extending a hot, thin lithosphere (80 km total, 40 km mantle lithosphere). This approach follows previous studies indicating that high extension velocity and weak lithosphere promote hyperextended, asymmetric rifting (e.g., Huismans and Beaumont, 2011; Brune et al., 2014; Tetreault and Buiter, 2018). We stop extension at the point of lithospheric breakup (i.e., first exposure of the asthenosphere) or halfway to the point of breakup in terms of time.

For each of these initial rift structures, we then vary the duration of post-rift cooling, during which horizontal velocities are set to 0. One set of models has no post-rift cooling phase (i.e., immediate inversion following extension), while a second set has a cooling period of 20 Myr. For each of the resulting 8 combinations of rift structure and post-rift cooling, we impose 2 different convergence velocities during inversion (1 cm/yr, 5 cm/yr) that capture a range of typical convergent plate motion (e.g., Hatzfeld and Molnar, 2010), with inversion duration scaled (20 Myr, 4 Myr) so that each resulting orogen undergoes the same amount of total convergence (200 km). This allows direct comparison of orogenic style across models independent of the stage of orogenic evolution.

Model Limitations

Our limited parameter sweep naturally excludes many possible rift geometries, post-rift cooling durations, and convergence velocities while seeking to establish first-order impacts these variables may have on the resulting orogens. In particular, we only examine rift inversion orogens resulting from rifts that have not been extended beyond the point of lithospheric breakup. We do not model this scenario specifically because our models do not account for magmatism and the resulting production of oceanic lithosphere, which may significantly impact rheology and strain localization.

<u>Summary of Model Tests</u>

We conducted extensive tests of a reference rift inversion model to determine the optimal balance between model realism, stability, and computational efficiency in ASPECT. All model tests involved 12.5 Myr of extension at 1 cm/yr with a mantle lithosphere of 60 km thickness to bring a continental rift to breakup, followed by 20 Myr of inversion at 1 cm/yr (200 km shortening) to create a model orogen. The inversion phase in particular was prone to crashing with convergence errors in the linear solver of ASPECT as one side of the orogen was thrust beneath another, necessitating a careful choice of parameters that would allow underthrusting to take place successfully.

To increase model realism, we attempted to implement a viscoelastic-plastic rheological formulation, but this resulted in model instability when combined with particle-in-cell material tracking methods and composite creep in the asthenosphere. For the long-duration, lithosphere-scale models presented here, the latter two features are most essential for enabling comparison with real-world orogens; thus, we adopted a viscoplastic rheology.

We tested increasing the range of permissible viscosities from 1 x 10^{18} Pa s to 1 x 10^{26} Pa s but found that the large viscosity contrasts led to convergence errors and model instability when coupled with composite creep in the asthenosphere. Models ran most efficiently at a range of 1 x 10^{20} Pa s to 1 x 10^{26} Pa s, but we adopt the more realistic, but still acceptably efficient range of 1 x 10^{19} Pa s to 1 x 10^{25} Pa s.

We attempted to increase the efficiency and accuracy of the particle-in-cell material tracking by using a bilinear least square interpolation scheme but found that, in the absence of a limiter, tracking of compositional fields on the model sides became highly inaccurate, with runaway increases in values that should not have exceeded 1. Instead, we use a cell averaging scheme for particle interpolation. We also fix vertical velocities and compositions on the sides of the models, in addition to having all inflow/outflow at the sides rather than the base, to ensure no errors in assignment of compositional fields to new material flowing into the model domain.

We attempted to improve model efficiency and stability by employing adaptive mesh refinement (AMR), in which model resolution would be as low as 4 km in the asthenosphere and 1 km only in the crust and uppermost mantle. Although AMR improved model performance considerably and produced rifting models very similar to those at 1 km global resolution, there were significant differences in first-order structural style between inversion models with any component of AMR in a 1000 x 400 km model domain and inversion models with constant resolution (1 km) in a 1000 x 400 km model domain. As a result, here we use a model domain of 1000 x 600 km with AMR, which produces comparable results to the 1000 x 400 km model with 1 km global resolution.

Comparisons with Prior Rift Inversion Models

Our study differs from prior work primarily in seeking to explore the range of structural variability in rift inversion orogenesis as a general process, rather than investigating a specific rift-inversion orogen or comparing rift-inversion models with compressional models that have no extension phase. Many prior modeling studies focus on recreating the present-day structure of the Pyrenees (Jammes et al., 2014; Dielforder et al., 2019; Jourdon et al., 2019). These studies thus explore a limited parameter space and report models either without altering initial rift state or convergence velocity (Dielforder et al., 2019) or with only minor variations in magnitude of extension and/or crustal rheology (Jammes et al., 2014; Jourdon et al., 2019). These models produced hyperextended rifts and rift-inversion orogens with significant asymmetric underthrusting comparable to the Pyrenees (Style AU), but the limited parameter space makes it difficult to identify the variables controlling the orogen asymmetry.

A few additional modeling studies have looked at rift-inversion orogenesis across a wider and more general parameter space. One compares model orogens formed from compression of a uniform lithospheric block with those formed from inversion after 100 km of extension, with variations in crustal rheology and erosion (Jammes and Huismans, 2012). A second study similarly imposes 150 km of extension on a single model to compare resulting orogenic structure with models compressing a coherent lithospheric block (Wolf et al., 2021). The first-order structures of the resulting orogens in both studies are comparable to their compression-only counterparts, though the inversion models do create wider orogens with more mantle upwelling. A third study, strongly motivated by the structure of the High Atlas, inverts a symmetric rift after 70 km of extension, varying the post-rift cooling, the erosion rate during inversion, and the rheological properties of sediment deposited in the rift (Buiter et al., 2009). These models produce orogens exhibiting distributed lithospheric thickening (Style DT), with greater reactivation of the major rift-bounding normal faults being promoted by hotter thermal states, faster erosion, and weaker sediment. Although some restricted parameter space is explored in these examples, the range of variation is limited such that models do not vary significantly in terms of their first-order structural style.

Our models also differ from many prior rift-inversion models in terms of how brittle strain softening is modeled, with prior studies using initial-reduced internal friction angles of 15°-2° (Jammes and Huismans, 2012; Jammes et al., 2014; Wolf et al., 2021), 30°-6° (Jourdon et al., 2019), and ~ 31.30°-2.87° (Dielforder et al., 2019). The weakened values in these ranges, particularly those of all studies other than Jourdon et al. (2019), represent the lower end of commonly assumed weakened values (see Naliboff et al., 2017 and 2020 for further discussion). The weakening parameterization is particularly significant for rift inversion problems, as absent strain healing, large portions of the lithosphere may have a significantly reduced brittle strength at the onset of compression. These lower weakened values in prior work may contribute to wider zones of deformation in the resulting orogen (>200 km wide) compared with our model results (~100 km wide) at similar magnitudes of convergence.

Model Parameter Files and Code

ASPECT parameter files for each of the 16 model runs and Python code used to prepare model runs, analyze results, and construct figures are available in a GitHub repository (https://github.com/dyvasey/riftinversion) and will be archived with a DOI using Zenodo upon manuscript acceptance.

References

Bahadori, A. et al., 2022, Coupled influence of tectonics, climate, and surface processes on landscape evolution in southwestern North America: Nature Communications, v. 13, p. 4437, doi:10.1038/s41467-022-31903-2.

Bangerth, W., Dannberg, J., Fraters, M., Gassmoeller, R., Glerum, A., Heister, T., and Naliboff, J., 2021, ASPECT v2.3.0:, https://doi.org/10.5281/ZENODO.5131909.

Brune, S., Heine, C., Pérez-Gussinyé, M., and Sobolev, S.V., 2014, Rift migration explains continental margin asymmetry and crustal hyper-extension: Nature Communications, v. 5, p. 4014, doi:10.1038/ncomms5014.

Brune, S., Kolawole, F., Olive, J.-A., Stamps, D.S., Buck, W.R., Buiter, S.J.H., Furman, T., and Shillington, D.J., 2023, Geodynamics of continental rift initiation and evolution: Nature Reviews Earth & Environment, v. 4, p. 235–253, doi:10.1038/s43017-023-00391-3.

Chapman, D.S., 1986, Thermal gradients in the continental crust: Geological Society, London, Special Publications, v. 24, p. 63–70, doi:10.1144/GSL.SP.1986.024.01.07.

Dielforder, A., Frasca, G., Brune, S., and Ford, M., 2019, Formation of the Iberian-European convergent plate boundary fault and its effect on intraplate deformation in Central Europe: Geochemistry, Geophysics, Geosystems, v. 20, p. 2395–2417, doi:10.1029/2018GC007840.

Fraters, M.R.T., and Billen, M.I., 2021, On the implementation and usability of crystal preferred orientation evolution in geodynamic modeling: Geochemistry, Geophysics, Geosystems, v. 22, p. e2021GC009846, doi:10.1029/2021GC009846.

Gleason, G.C., and Tullis, J., 1995, A flow law for dislocation creep of quartz aggregates determined with the molten salt cell: Tectonophysics, v. 247, p. 1–23, doi:10.1016/0040-1951(95)00011-B.

Glerum, A., Brune, S., Stamps, D.S., and Strecker, M.R., 2020, Victoria continental microplate dynamics controlled by the lithospheric strength distribution of the East African Rift: Nature Communications, v. 11, p. 2881, doi:10.1038/s41467-020-16176-x.

Glerum, A., Thieulot, C., Fraters, M., Blom, C., and Spakman, W., 2018, Nonlinear viscoplasticity in ASPECT: Benchmarking and applications to subduction: Solid Earth, v. 9, p. 267–294, doi:10.5194/se-9-267-2018.

Gouiza, M., and Naliboff, J., 2021, Rheological inheritance controls the formation of segmented rifted margins in cratonic lithosphere: Nature Communications, v. 12, p. 4653, doi:10.1038/s41467-021-24945-5.

Hatzfeld, D., and Molnar, P., 2010, Comparisons of the kinematics and deep structures of the Zagros and Himalaya and of the Iranian and Tibetan plateaus and geodynamic implications: Reviews of Geophysics, v. 48, p. RG2005, doi:10.1029/2009RG000304.

Heister, T., Dannberg, J., Gassmöller, R., and Bangerth, W., 2017, High accuracy mantle convection simulation through modern numerical methods – II: Realistic models and problems: Geophysical Journal International, v. 210, p. 833–851, doi:10.1093/gji/ggx195.

Heron, P.J., Peace, A.L., McCaffrey, K.J.W., Sharif, A., Yu, A.J., and Pysklywec, R.N., 2023, Stranding continental crustal fragments during continent breakup: Mantle suture reactivation in the Nain Province of Eastern Canada: Geology, v. 51, p. 362–365, doi:10.1130/G50734.1.

Hirth, G., and Kohlstedt, D., 2003, Rheology of the upper mantle and the mantle wedge: A view from the experimentalists: Geophysical Monograph-American Geophysical Union, v. 138, p. 83–106.

Huismans, R., and Beaumont, C., 2011, Depth-dependent extension, two-stage breakup and cratonic underplating at rifted margins: Nature, v. 473, p. 74–78, doi:10.1038/nature09988.

Jammes, S., and Huismans, R.S., 2012, Structural styles of mountain building: Controls of lithospheric rheologic stratification and extensional inheritance: Journal of Geophysical Research: Solid Earth, v. 117, doi:10.1029/2012JB009376.

Jammes, S., Huismans, R.S., and Muñoz, J.A., 2014, Lateral variation in structural style of mountain building: controls of rheological and rift inheritance: Terra Nova, v. 26, p. 201–207, doi:10.1111/ter.12087.

Jourdon, A., Le Pourhiet, L., Mouthereau, F., and Masini, E., 2019, Role of rift maturity on the architecture and shortening distribution in mountain belts: Earth and Planetary Science Letters, v. 512, p. 89–99, doi:10.1016/j.epsl.2019.01.057.

Kronbichler, M., Heister, T., and Bangerth, W., 2012, High accuracy mantle convection simulation through modern numerical methods: Geophysical Journal International, v. 191, p. 12–29, doi:10.1111/j.1365-246X.2012.05609.x.

Magni, V., Naliboff, J., Prada, M., and Gaina, C., 2021, Ridge jumps and mantle exhumation in back-arc basins: Geosciences, v. 11, p. 475, doi:10.3390/geosciences11110475.

Naliboff, J.B., and Buiter, S.J.H., 2015, Rift reactivation and migration during multiphase extension: Earth and Planetary Science Letters, v. 421, p. 58–67, doi:10.1016/j.epsl.2015.03.050.

Naliboff, J.B., Buiter, S.J.H., Péron-Pinvidic, G., Osmundsen, P.T., and Tetreault, J., 2017, Complex fault interaction controls continental rifting: Nature Communications, v. 8, p. 1179, doi:10.1038/s41467-017-00904-x.

Naliboff, J.B., Glerum, A., Brune, S., Péron-Pinvidic, G., and Wrona, T., 2020, Development of 3-D rift heterogeneity through fault network evolution: Geophysical Research Letters, v. 47, p. e2019GL086611, doi:https://doi.org/10.1029/2019GL086611.

Pan, S., Bell, R.E., Jackson, C.A.-L., and Naliboff, J., 2022, Evolution of normal fault displacement and length as continental lithosphere stretches: Basin Research, v. 34, p. 121–140, doi:10.1111/bre.12613.

Rose, I., Buffett, B., and Heister, T., 2017, Stability and accuracy of free surface time integration in viscous flows: Physics of the Earth and Planetary Interiors, v. 262, p. 90–100, doi:10.1016/j.pepi.2016.11.007.

Rybacki, E., Gottschalk, M., Wirth, R., and Dresen, G., 2006, Influence of water fugacity and activation volume on the flow properties of fine-grained anorthite aggregates: Journal of Geophysical Research: Solid Earth, v. 111, doi:https://doi.org/10.1029/2005JB003663.

Sandiford, D., Brune, S., Glerum, A., Naliboff, J., and Whittaker, J.M., 2021, Kinematics of Footwall Exhumation at Oceanic Detachment faults: Solid-Block Rotation and Apparent Unbending: Geochemistry, Geophysics, Geosystems, v. 22, p. e2021GC009681, doi:10.1029/2021GC009681.

Tetreault, J.L., and Buiter, S.J.H., 2018, The influence of extension rate and crustal rheology on the evolution of passive margins from rifting to break-up: Tectonophysics, v. 746, p. 155–172, doi:10.1016/j.tecto.2017.08.029.

Weerdesteijn, M.F.M., Naliboff, J.B., Conrad, C.P., Reusen, J.M., Steffen, R., Heister, T., and Zhang, J., 2023, Modeling Viscoelastic Solid Earth Deformation Due To Ice Age and Contemporary Glacial Mass Changes in ASPECT: Geochemistry, Geophysics, Geosystems, v. 24, p. e2022GC010813, doi:10.1029/2022GC010813.

Wolf, S.G., Huismans, R.S., Muñoz, J.-A., Curry, M.E., and Beek, P. van der, 2021, Growth of Collisional Orogens From Small and Cold to Large and Hot—Inferences From Geodynamic Models: Journal of Geophysical Research: Solid Earth, v. 126, p. e2020JB021168, doi:https://doi.org/10.1029/2020JB021168.

Table S1: Material Properties for Compositional Layers

	Upper Crust	Lower Crust	Mantle Lithosphere	Asthenosphere[1]	
Density (kg m^{-3})	2800	2900	3300	3300	
Flow Law[2]	Wet quartzite	Wet anorthite	Dry olivine	Dry olivine (dislocation)	Dry olivine (diffusion)
Viscosity Prefactor (A) (Pa^{-n} m^{-p} s^{-1})	8.57 x 10^{-28}	7.13 x 10^{-18}	6.52 x 10^{-16}	6.52 x 10^{-16}	2.37 x 10^{-15}
Stress exponent (n)	4	3	3.5	3.5	-
Grain size (d) (m)	-	-	-	-	1 x 10^{-3}
Grain size exponent (m)	-	-	-	-	3
Activation energy (Q) (kJ mol^{-1})	223	345	530	530	375
Activation volume (V) (m^3 mol^{-1})	-	-	-	-	18 x 10^{-6}
Specific heat (Cp) (J kg^{-1} K^{-1})	750	750	750	750	
Thermal conductivity (κ) (W m^{-1} K^{-1})	2.5	2.5	2.5	2.5	
Thermal expansivity (α) (K^{-1})	2 x 10^{-5}	2 x 10^{-5}	2 x 10^{-5}	2 x 10^{-5}	
Heat production (H) (W m^{-3})	1 x 10^{-6}	0.25 x 10^{-6}	0	0	
Friction angle[3] (°)	30	30	30	30	
Cohesion[3] (MPa)	20	20	20	20	

1. Asthenosphere viscous rheology determined by harmonic averaging of dislocation and diffusion creep flow laws.
2. Source for flow laws: wet quartzite (Gleason and Tullis, 1995), wet anorthite (Rybacki et al., 2006), dry olivine (Hirth and Kohlstedt, 2003).
3. Friction angle and cohesion decrease linearly by a factor of 0.375 between plastic strain values of 0.5 and 1.5 to simulate strain weakening.

Table S2: Model Pairs in which 1 Variable Is Changed

Model comparisons showing impact of rift mechanics (0.5 vs. 2 cm/yr Extension Velocity)

Model Pair	Extension Velocity (varied)	Rift Duration	Post-Rift Cooling	Inversion Velocity
1,5	0.5 or 2 cm/yr	Halfway (16 Myr)	0 Myr	1 cm/yr
2,6	0.5 or 2 cm/yr	Halfway (16 Myr)	20 Myr	1 cm/yr
3,7	0.5 or 2 cm/yr	Full Breakup (32 Myr)	0 Myr	1 cm/yr
4,8	0.5 or 2 cm/yr	Full Breakup (32 Myr)	20 Myr	1 cm/yr
9,13	0.5 or 2 cm/yr	Halfway (16 Myr)	0 Myr	5 cm/yr
10,14	0.5 or 2 cm/yr	Halfway (16 Myr)	20 Myr	5 cm/yr
11,15	0.5 or 2 cm/yr	Full Breakup (14.5 Myr)	0 Myr	5 cm/yr
12,16	0.5 or 2 cm/yr	Full Breakup (14.5 Myr)	20 Myr	5 cm/yr

Model comparisons showing impact of rift duration (halfway vs. full breakup)

Model Pair	Extension Velocity	Rift Duration (varied)	Post-Rift Cooling	Inversion Velocity
1,3	0.5 cm/yr	Halfway or Full Breakup	0 Myr	1 cm/yr
2,4	0.5 cm/yr	Halfway or Full Breakup	20 Myr	1 cm/yr
5,7	2 cm/yr	Halfway or Full Breakup	0 Myr	1 cm/yr
6,8	2 cm/yr	Halfway or Full Breakup	20 Myr	1 cm/yr
9,11	0.5 cm/yr	Halfway or Full Breakup	0 Myr	5 cm/yr
10,12	0.5 cm/yr	Halfway or Full Breakup	20 Myr	5 cm/yr
13,15	2 cm/yr	Halfway or Full Breakup	0 Myr	5 cm/yr
14,16	2 cm/yr	Halfway or Full Breakup	20 Myr	5 cm/yr

Model comparisons showing impact of post-rift cooling (0 vs. 20 Myr)

Model Pair	Extension Velocity	Rift Duration	Post-Rift Cooling (varied)	Inversion Velocity
1,2	0.5 cm/yr	Halfway (16 Myr)	0 or 20 Myr	1 cm/yr
3,4	0.5 cm/yr	Full Breakup (32 Myr)	0 or 20 Myr	1 cm/yr
5,6	2 cm/yr	Halfway (7.3 Myr)	0 or 20 Myr	1 cm/yr
7,8	2 cm/yr	Full Breakup (14.5 Myr)	0 or 20 Myr	1 cm/yr
9,10	0.5 cm/yr	Halfway (16 Myr)	0 or 20 Myr	5 cm/yr
11,12	0.5 cm/yr	Full Breakup (32 Myr)	0 or 20 Myr	5 cm/yr
13,14	2 cm/yr	Halfway (7.3 Myr)	0 or 20 Myr	5 cm/yr
15,16	2 cm/yr	Full Breakup (14.5 Myr)	0 or 20 Myr	5 cm/yr

Model comparisons showing impact of convergence velocity (1 vs. 5 cm/yr)

Model Pair	Extension Velocity	Rift Duration	Post-Rift Cooling	Inversion Velocity (varied)
1,9	0.5 cm/yr	Halfway (16 Myr)	0 Myr	1 or 5 cm/yr
2,10	0.5 cm/yr	Halfway (16 Myr)	20 Myr	1 or 5 cm/yr
3,11	0.5 cm/yr	Full Breakup (32 Myr)	0 Myr	1 or 5 cm/yr
4,12	0.5 cm/yr	Full Breakup (32 Myr)	20 Myr	1 or 5 cm/yr
5,13	2 cm/yr	Halfway (7.3 Myr)	0 Myr	1 or 5 cm/yr
6,14	2 cm/yr	Halfway (7.3 Myr)	20 Myr	1 or 5 cm/yr
7,15	2 cm/yr	Full Breakup (14.5 Myr)	0 Myr	1 or 5 cm/yr
8,16	2 cm/yr	Full Breakup (14.5 Myr)	20 Myr	1 or 5 cm/yr

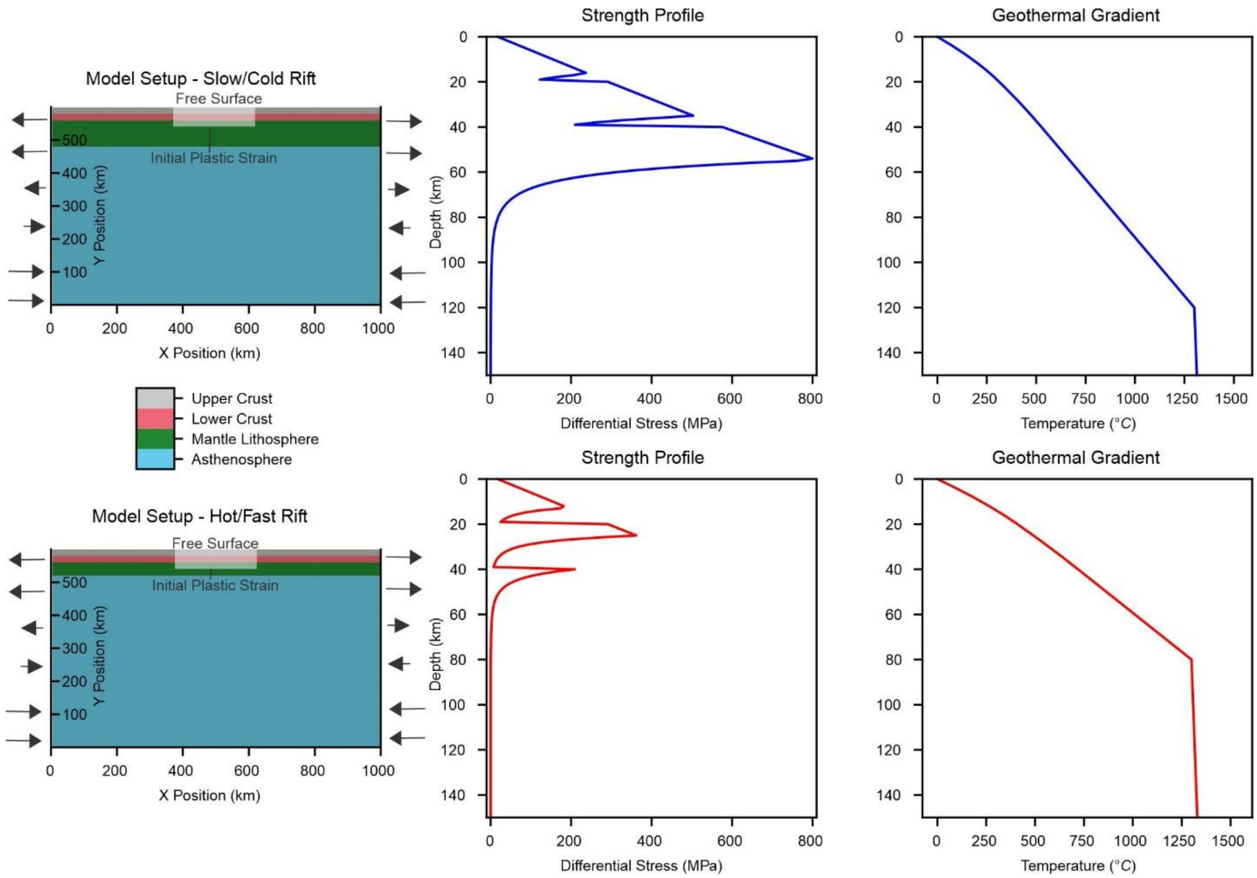

Figure S1: Initial conditions for rift inversion models with a slow, cold rift (top row) and hot, fast rift (bottom row). Models consist of a 1000x600 km box divided into compositional fields for upper crust, lower crust, mantle lithosphere, and asthenosphere, with total lithosphere thickness of 120 km in slow, cold models and 80 km in hot, fast models. Arrows on either side of the setup diagrams show material flow directions during the rifting phase, with outflow on the model sides in the top half of the model is balanced from inflow on the model sides in the bottom half of the model. A 250x60 km zone of randomized initial plastic strain (gray box) helps localize strain in the center of the model. Effective strength, shown for a reference strain rate of 1 x 10^{-15} s^{-1}, is a combination of dislocation/diffusion creep viscous rheology and Drucker-Prager plasticity (Table S1); the geothermal gradient is modified by changing surface heat flow so that the base of the lithosphere is at 1300°C.

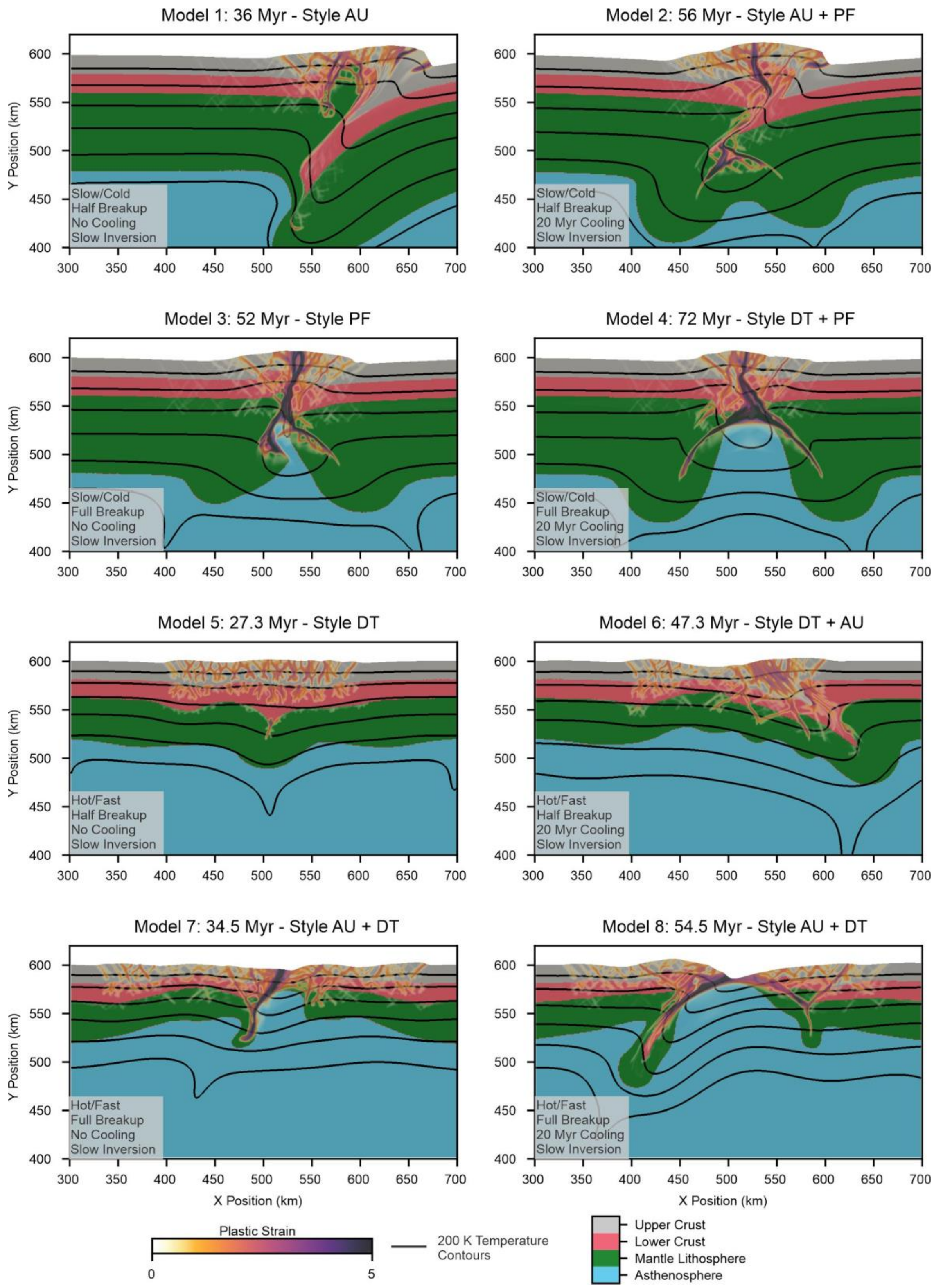

Figure S2: Final model orogen results (200 km convergence) for all models with a convergence velocity of 1 cm/yr.

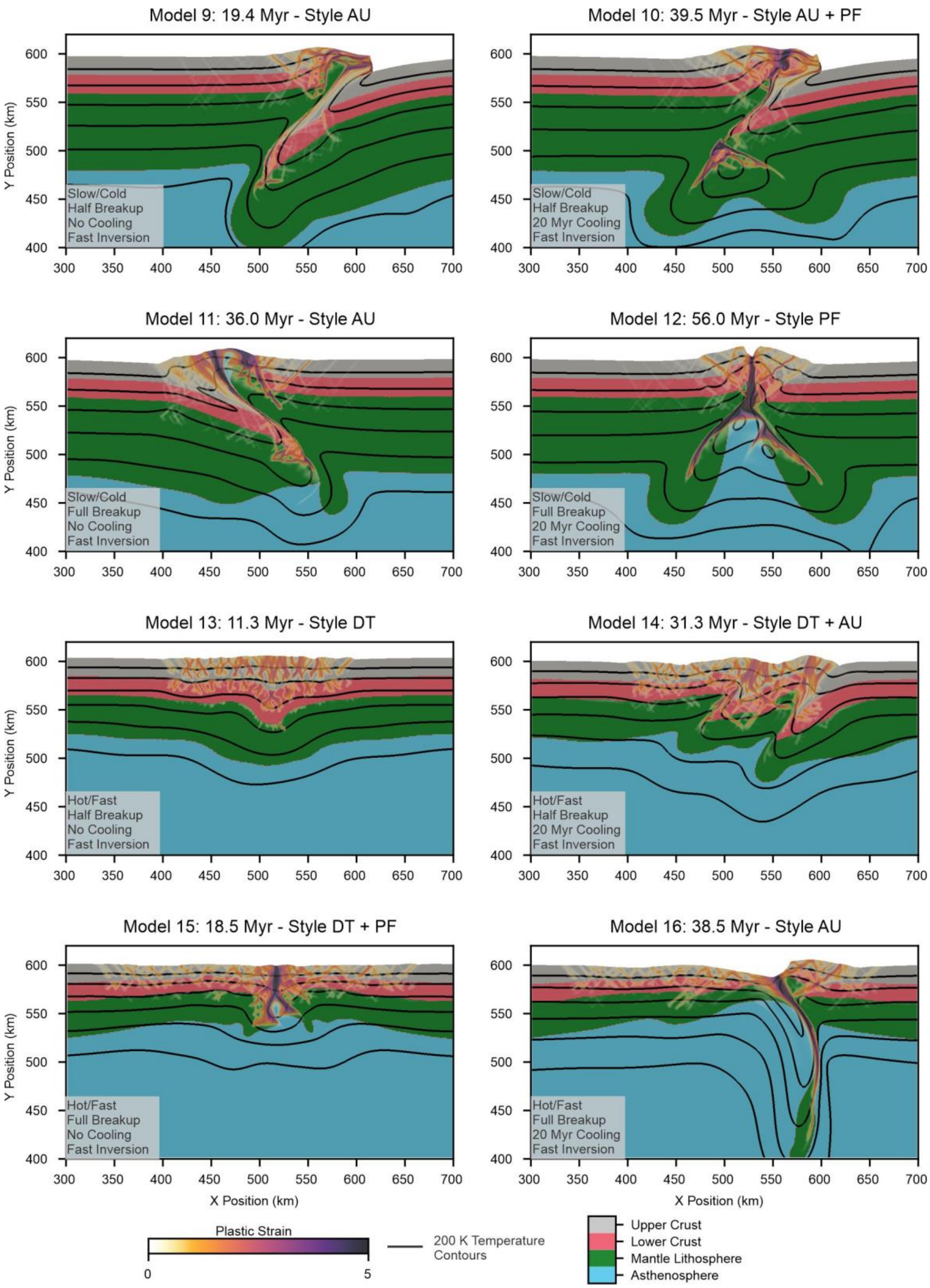

Figure S3: Final model orogen results (200 km convergence) for all models with a convergence velocity of 5 cm/yr.